ELSEVIER

International Journal of Mass Spectrometry 177 (1998) 91–104

International Journal of Mass Spectrometry

Characteristics of a broad-band Fourier transform ion trap mass spectrometer

Mario Nappi, Vladimir Frankevich, Manish Soni, R. Graham Cooks*

Department of Chemistry, Purdue University, West Lafayette, IN 47907, USA

Received 3 November 1997; accepted 14 April 1998

Abstract

The characteristics of a novel Fourier transform ion trap mass spectrometer capable of broadband nondestructive ion detection are described. Details of the instrumentation, including the custom-built detection circuitry, are provided. An approximate mathematical model for the image current signal-to-noise ratio is derived from the work of Comisarow [J. Chem. Phys. 69 (1978) 4097] and used to estimate the sensitivity of the technique. Data obtained using impulsive dc excitation and ac excitation are presented and frequency shifts, mass calibration, mass resolution and sensitivity are discussed. The detrimental effects of space charging and nonlinear fields on performance are examined using experimental data and computer simulations. The effect of dc biasing on ion frequency and signal intensity is investigated and mass calibration data are presented. (Int J Mass Spectrom 177 (1998) 91–104) © 1998 Elsevier Science B.V.

Keywords: Ion trap; Fourier transform; Nondestructive detection; Simulations; Ion motion; Quadrupole field

Introduction

Early ion trap experiments of Paul et al.[1], Fischer [2], and Rettinghaus [3] employed in situ methods of ion detection. These methods involved measurement of the power absorbed by resonant ions. Using variations on these approaches, Parks et al. [4] and Goeringer et al. [5] more recently demonstrated improved performance in nondestructive detection of ions using image current measurements. A major drawback of all these techniques is the inherently narrow detection bandwidth that prevents the simultaneous measurement of ions covering a wide mass range.

Commercial ion traps use a simple and sensitive ion detection method that involves mass-selective ejection of ions into an external detector. The mass-selective instability scan mode used [6] involves slowly ramping the rf trapping voltage to bring ions sequentially into axial instability. This is usually done under the influence of a supplementary dipolar ac signal applied in the z-direction. The ions achieve resonance with the supplementary field, become unstable, exit the trap through an aperture in the endcap electrode and strike the external detector, usually a conversion dynode/electron multiplier combination. The signal generated at the detector is recorded as a function of the rf voltage to obtain the mass spectrum. Because ions are lost once they strike the detector surface, ion detection is destructive.

* Corresponding author.

1387-3806/98/$19.00 © 1998 Elsevier Science B.V. All rights reserved
PII S1387-3806(98)14038-1

Recently, we reported a new nondestructive ion detection method for the ion trap mass spectrometer (ITMS) that, for the first time, allows broad-band ion detection [7]. In this Fourier transform (FT)-ITMS experiment, an auxiliary detector electrode is used to receive image currents from a coherently oscillating ion population. Coherent ion excitation is achieved using simple dc (impulsive) excitation or resonant narrow-band ac or broadband stored waveform inverse Fourier transform [8,9] (SWIFT) excitation. The induced image currents are measured using a home-built broadband detection circuit and Fourier analyzed to yield the corresponding mass spectra. Image current measurement followed by Fourier analysis in ion trap mass spectrometry was first reported by Syka and Fies over a narrow bandwidth [10]. The present FT-ITMS technique is broadband and resembles FT ion cyclotron resonance [11] (ICR) with which it shares many advantages. For example, it allows a single ion population to be measured multiple times (ion remeasurement) and improvements in signal-to-noise (S/N) ratios can be achieved via data averaging or summing [12]. The same ions can be studied further by using tandem mass spectrometry or ion/molecule reactions. Some results demonstrating these capabilities have already been reported [7].

This follow-up article provides details about the FT-ITMS experimental setup and the custom-built detection circuitry. It addresses the fundamental issues of frequency shifts, mass calibration, mass resolution, and sensitivity. The influence of space-charge and higher-order fields is discussed using computer simulations and experimental data. The complex nature of these effects makes precise mass calibration difficult, but an empirical mass-calibration law based on experimental data is presented. Image current S/N ratios are expressed using equations derived from Comisarow's FT-ICR model [13] and used to estimate the detection sensitivity. The effects of dc biasing of the ion trap to manipulate ion clouds during detection are discussed. Finally, a dual detector-electrode FT-ion trap design is proposed to correct for some of the nonlinear field effects encountered in the current design and to decrease noise.

Experimental

Instrumentation

A schematic diagram of the instrumental arrangement is shown in Fig. 1. All experiments were performed using internal electron ionization (EI) in a prototype Finnigan ITMS (Finnigan Corp., San Jose, CA) that has been described previously [14]. A 3.2 mm $\times$ 32.5 mm (diameter $\times$ length) detector stainless-steel electrode was mounted in the exit endcap electrode using an insulating teflon support. For impulsive ion excitation, a 2 ms/10−80 V pulse having rise and fall times of 10 and 20 ns, respectively, was applied to the endcap electrodes using a fast dc pulser (DEI, Fort Collins, CO). The dc pulse was not phase-locked to the main rf trapping voltage. Resonant ion excitation was performed in the narrow-band mode, using single frequency ac signals, and in the broadband mode, using SWIFT pulses. The SWIFT pulses were created and applied as reported previously [9,15] by using an arbitrary waveform generator (ARB, Model 395, Wavetek Corp., San Diego, CA). The excitation signal was applied only to the entrance endcap electrode in these experiments; however, it can be applied across both the entrance and exit endcaps in a dipolar fashion without any further modifications.

The standard ITMS data system and electronics were used to control the operation of the ion trap and provide the necessary trigger sequence for operation of various auxiliary devices. A delay generator (Model DG535, S.R.S. Corp., Sunnyvale, CA) was used to provide the necessary delays for sequential triggering of the devices. The image currents induced on the detector electrode were measured by using a simple preamplifier-filter-amplifier arrangement described below. The amplified signal was observed using a digital oscilloscope (Model TDS 540, Tektronix, Beaverton, OR) set at 1 MHz sampling frequency, 1 MΩ input impedance and 15k data points horizontal resolution to yield a data-acquisition window of 15 ms. An acquisition window of 50 ms (50k data points at 1 MHz) was used for some experiments, as indicated.

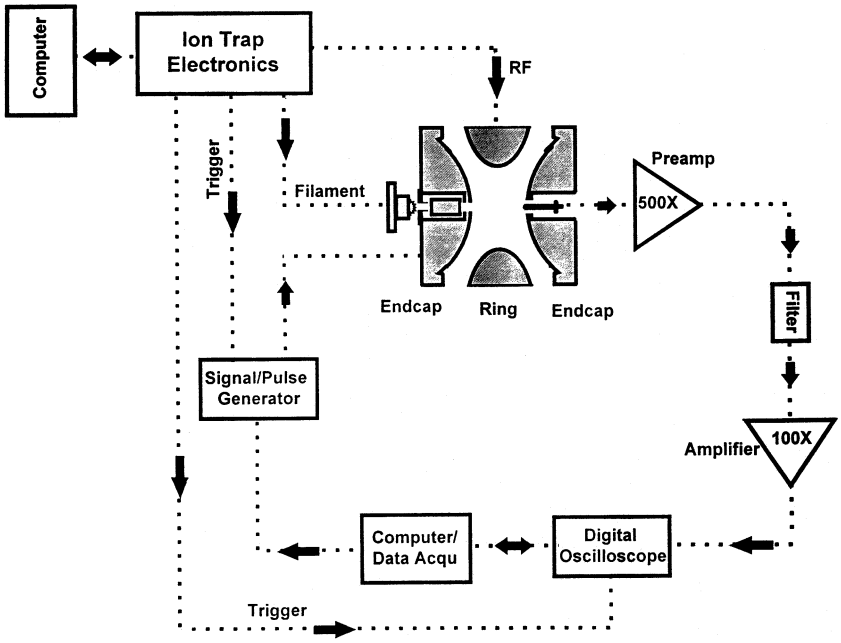

Fig. 1. Experimental arrangement used for broadband nondestructive Fourier transform ion trap mass spectrometry.

The oscilloscope was operated in the signal averaging mode (running average over 100 scans) for all experiments. The built-in real-time fast Fourier transform (FFT) capability of the oscilloscope was used during tuning, whereas optimized time-domain transients were downloaded to a computer with a general purpose interface board (GPIB) interface for further FFT processing and background subtraction using STATMOST, a statistical spreadsheet program (ver 2.1, Datamost Corp., Salt Lake City, UT). Background signals were recorded under identical conditions, except that the excitation source was turned off. These spectra were subtracted from sample spectra to remove systematic noise signals and so improve S/N ratios. Nominal mass assignments were made by manually calculating the mass-to-charge ratio value for each peak in the frequency domain using the Mathieu equations [16]. All samples were directly leaked into the ion trap manifold through a leak valve (Granville-Phillips, Boulder, CO) to obtain a pressure reading in the range of $0.4 - 3 \times 10^{-6}$ Torr (uncorrected). No helium bath gas was used in recording the spectra reported here.

Detection circuit

The detection circuit consists of a preamplifier and a commercially available analog filter/amplifier (Model 4302, ITHACO, Ithaca, NY). To minimize stray capacitance at the preamp input, the detector electrode was connected to the preamplifier using short, shielded, vacuum-compatible coaxial leads which extend outside the vacuum manifold through a conflat-flange feed-through. The preamplifier is home-built and consists of two stages, as shown in Fig. 2. The first stage is a Burr-Brown INA-111 differential-instrumentation amplifier with 10 MΩ resistance at each input. For the experiments described here, one of the inputs to the differential amplifier was connected to the detector electrode, whereas the other was grounded. The first stage has a gain of 10 and is followed by a single-pole RC network with a high-frequency breakpoint of 500 kHz. A negative feedback technique is used to set the low-frequency cutoff to 10 kHz. The final stage of the preamp is another Burr-Brown differential amplifier set to provide a gain of 50. The preamp provides a

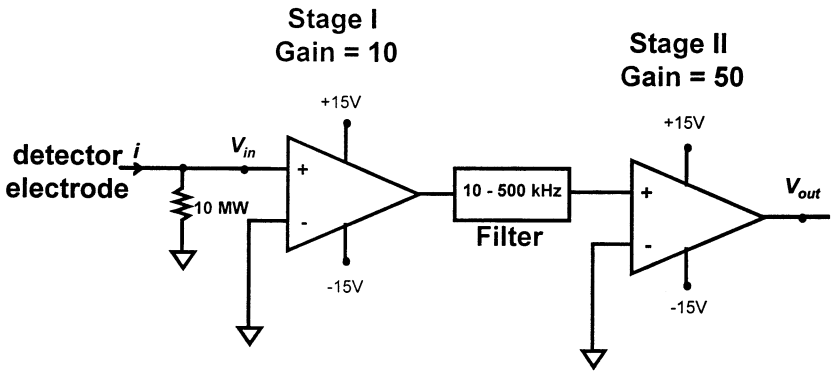

Fig. 2. Schematic of the home-built preamplifier circuit.

total gain of 500 and a current-transfer ratio of 5 $mV_{0\text{-}p}$ (output) per 1 pA current (input) at 500 kHz bandwidth. The preamp unit is powered by a bipolar 15 V power supply taken directly from the ITMS analog board (terminals JC2 and JC3). To reduce noise from the power supply, a dc voltage transformer was used as an isolating transformer to isolate the preamp from the 15 V ITMS power supply, i.e. to prevent the transmission of any ac noise from the power source to the preamp. The output of the preamp is fed into the analog filter/amplifier which is set at 100 gain and 400 kHz bandwidth. The detection bandwidth is thus 400 kHz in the broad-band mode and is set to 25 kHz at the analog filter for narrow-band data acquisition.

Scan sequence

The timing sequence or scan function used to record a mass spectrum consists of an ionization stage (0.8–32 ms) followed by a 10–30 ms delay period for ion cooling and baseline stabilization followed by the excitation period during which the dc pulser (or the ARB) is triggered to apply the excitation signal. The dc excitation time was 2 μs whereas the SWIFT excitation period was 8 or 16 ms (1 or 2 pulses). Data were acquired (normally 15 ms per transient) using the oscilloscope to record the ion image signal. The rf amplitude was kept constant throughout this sequence of events at a value that corresponds to a low mass cutoff in the range of m/z 10–40. For ion remeasurement, the excitation/data acquisition sequence was performed multiple times. Ion isolation and CID stages were added for the tandem mass spectrometry experiments [7].

Results and discussion

Broadband and narrow-band mass spectra

Most experiments employed broadband excitation and detection but narrow-band excitation and detection were options used in some cases. An example of a broadband spectrum of xenon, obtained using broadband (viz. dc) excitation, image current detection and FT, is shown in Fig. 3. The spectrum shown is background subtracted and displays the characteristic Xe^+ ions at m/z 129, 130, 131, 132, 134, and 136 in isotopic ratios that approximately match their natural abundances, viz. 26.4%, 4.1%, 21.2%, 26.9%, 10.4%, and 8.9%, respectively. An example of a mass spectrum recorded using narrow-band detection (25 kHz detection bandwidth) after broadband dc excitation is shown in Fig. 4. It shows background subtracted mass spectra for acetophenone at two different pressures. The parent ion (M^+) occurs at m/z 120 and the $(M+H)^+$ ion, due to self-protonation, occurs to result in m/z 121, as is commonly the case in ion traps that use internal ionization. The abundance of protonated acetophenone increases at higher sample pressure (Fig. 4B), as expected.

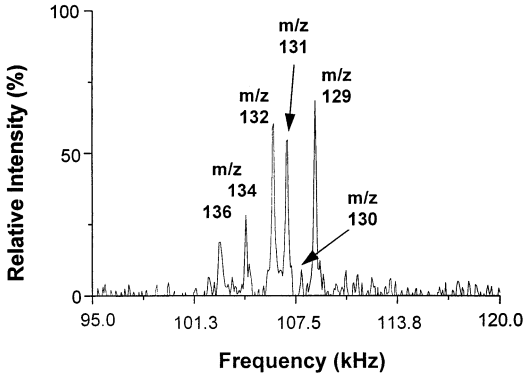

Fig. 3. Broadband mass spectrum of xenon (Xe^+) ions. Low mass/charge cutoff, m/z 40; ionization time, 0.9 ms; excitation by dc pulse, 50V, 2 μs; nominal pressure, 2×10^{-6} Torr.

S/N calculations

The image signal in the present system can be approximately described using the "rotating monopole" model proposed by Comisarow for ICR [13]. Based on this model, the charge (Q) induced in an electrode of area A by an oscillating ion cloud is given by

$$Q(t) = -\frac{NqzA}{V}\cos(\omega t), \tag{1}$$

where N is the number of coherently moving ions, z is the radius of ion oscillation (i.e. the displacement from the center in the z direction), q is the charge and ω is the ion secular frequency in radians/s. For simplicity of calculation, the total space within which ions oscillate in the axial dimension is approximated as a cylinder (volume V) with the detectors being represented by the two circular ends (area A) of the cylinder. Thus $A/V = 1/(2z_0)$, where z_0 is the center-to-endcap electrode distance.

The current i_s is then given by

$$i_s(t) = \frac{dQ}{dt} = \frac{Nqz}{2z_0}\,\omega\,\sin(\omega t) \tag{2}$$

or

$$i_s(\text{rms}) = \frac{Nqz}{2z_0\sqrt{2}}\,\omega \tag{3}$$

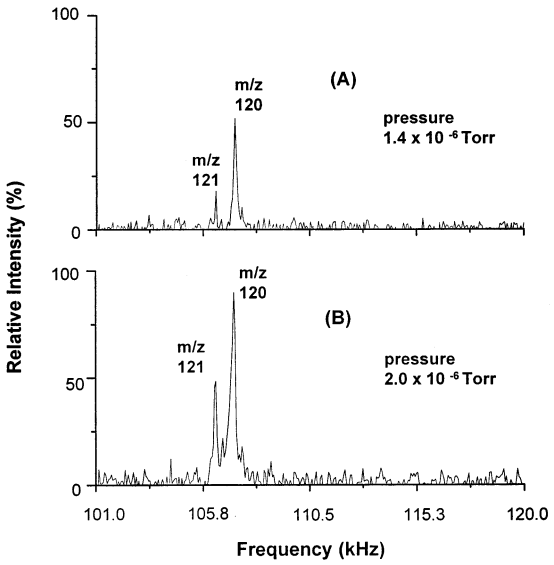

Fig. 4. Narrow-band (25 kHz) mass spectra of acetophenone showing the $M^{+\cdot}$ and $(M+H)^+$ ions at two different sample pressures. Low mass/charge cutoff, m/z 37; ionization time, 1.6 ms; broadband excitation by dc pulse, 30 V, 2 μs.

The corresponding image signal voltage can be given as

$$v_s(t) = i_s(t)\,Z \tag{4}$$

where

$$Z^2 = \left(\frac{1}{R^2} + \omega^2C^2\right)^{-1} \tag{5}$$

and Z is the impedance of the detection circuit consisting of parallel R and C elements and where R is the input resistance of the preamp and C is the ion trap capacitance. Thus, the magnitude of the image signal (v_s) is given by

$$v_s(\text{rms}) = \frac{Nqz\omega}{2\sqrt{2}\,z_0\,\sqrt{(1/R^2) + \omega^2C^2}} \tag{6}$$

For a Johnson-noise-limited measurement, the noise equals

$$v_n(\text{rms}) = \frac{\sqrt{4kT\Delta f\,(1/R)}}{\sqrt{(1/R^2) + \omega^2C^2}} \tag{7}$$

where k is the Boltzmann constant. The noise voltage is a function of the temperature, usually the ambient operating temperature of the first element of the

detection circuit, and of the equivalent input resistance of the preamp and its frequency bandwidth, Δf. The S/N is thus,

$$(\mathrm{S/N}) = v_s(\mathrm{rms})/v_n(\mathrm{rms}) = \frac{Nqz\omega}{2\sqrt{2}z_0\sqrt{4kT\Delta f(1/R)}} \quad (8)$$

When the ion cloud oscillates to 50% of its maximum possible displacement ($z/z_0 = 0.5$) and has a secular linear frequency of 180 kHz, and when $R = 10$ MΩ, $\Delta f = 400$ kHz, and $T = 298$ K, the theoretical value of N for S/N = 2 is 1800 ions. Experimentally, the intensity of the argon (m/z 40) signal, measured at this secular frequency, was found to be approximately 80 mV(rms) at S/N 5 by using the oscilloscope; the expectation value at S/N = 2 is therefore 26 mV. Using the theoretical current-to-voltage transfer ratio of the detection circuit, 26 mV (rms) $\approx 0.92 \times 10^{-13}$ A current at the detector. A current of $\sim 1 \times 10^{-13}$ A is therefore found, from the measurement, to give S/N 2. Thus, in a simple experiment that employs minimal signal averaging, a few thousand ions is expected to give a detectable signal in a broadband spectrum recorded using the parameters described.

Improving S/N ratios

Signal averaging is the obvious route to improved S/N ratios. From Eq. (8) one can conclude that the S/N ratio can be improved by i) operating at a lower temperature (T), ii) exciting ions more strongly and increasing z/z_0, iii) operating at higher ion frequencies (ω) and, iv) decreasing detection bandwidth (Δf). Many of these parameters, like temperature (T), ion frequency (ω), and ion excursion (z), involve tradeoffs, whereas decreasing the bandwidth (Δf) is undesirable. Operation at higher ion secular frequency and with greater ion excursions has the undesirable effect of increasing the number and magnitude of component ion frequencies and increasing the contributions of higher order fields, respectively. Both effects complicate ion motion and reduce performance.

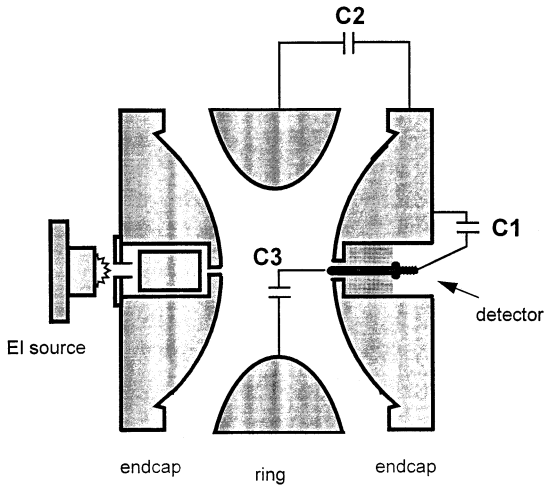

Fig. 5. Schematic of the modified ion trap showing the intrinsic capacitances that exist between the electrodes.

Minimizing rf contributions to the image current

The primary reason for using a small independent detector electrode in FT-ITMS is to minimize the pickup of the rf drive voltage by the detection circuit [7]. In ion traps, the high (kV range) rf trapping voltage is applied to the ring electrode and leaks into the image current detection circuit via the endcap electrodes. A balun or transformer is commonly used to isolate the supplementary dipolar excitation signal source from this residual rf current. The rf coupling occurs via the intrinsic capacitance (C_2) that exists between the endcap and the ring electrode (see Fig. 5). The rf image current is orders of magnitude larger than the image current from the oscillating ions, thus preventing direct measurements.

If C_1 is the capacitance between the detector and the endcap electrode and C_3 is the capacitance between the ring and the detector, the total capacitance of the trap, which is on the order of 10 pF, is given by

$$C = \frac{C_1C_2}{C_1 + C_2} + C_3 \quad (9)$$

Capacitive coupling through C_3 is smaller than C_2 because $C_3 < C_2$. This is because of the smaller surface area of the detector electrode and its larger distance from the ring electrode in comparison to that of the endcap itself. The capacitance between the

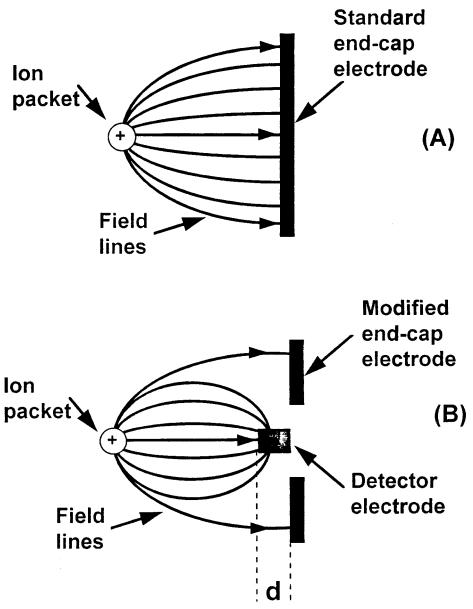

Fig. 6. The convergence of field-lines from oscillating ions on (A) endcap electrode and (B) detector electrode.

endcap and detector (C_1) is also assumed to be small. This reduces the rf leakage into the detection circuit and improves the signal/noise ratio. Experimentally, we have observed a reduction by a factor of 200 in rf pickup at the detector electrode compared to pickup by the entire endcap electrode [7]. In its current form, no additional electronic methods are used to minimize rf pickup. However, electronic rf nulling as achieved, for example, in the design of Syka and Fies [17], could be implemented in conjunction with use of the detector electrode, to further improve S/N ratios at high rf operating voltages.

Detector dimensions and placement

The dimensions of the pin electrode and its position with respect to the ion trap center are important parameters that affect S/N performance. The magnitude of the image signal can be increased by adjusting the position "d" (see Fig. 6) and/or by increasing the diameter of the detector electrode, but these parameters must be optimized as they also increase rf noise pickup. The signal produced by the oscillating ion packet is proportional to the number of electric field lines that terminate on the surface of the detector plate. The density of the field lines is proportional to the square of the distance between the plate and the ion packet and to its size. By optimizing the value of d, the collection of the field lines from the coherent ion population is maximized, as illustrated in Fig. 6. The field lines converge on the entire endcap electrode of large area in (A) and on the detector surface (smaller area) in (B). To minimize loss of field lines to the surrounding endcap, the area of the detector needs to be approximately the same as the cross-sectional area of the cylindrical volume occupied by the oscillating ion cloud. Electrodes with diameters 1.0, 1.6, and 3.2 mm were studied using various values of the position descriptor d, both positive and negative, where the positive sign is defined in Fig. 6. A pin electrode, diameter 3.2 mm, placed so that the dimension $d = +0.5$ mm, was determined to be a good compromise between signal gain and increased rf pickup. The physical isolation of the detector from the endcap electrode also eliminates the need for noisy switching circuits that would otherwise be required to alternate between ion excitation and image current detection stages of the experiment.

Frequency shifts and mass calibration

Systematic shifts between the experimental and calculated frequencies have been observed in all FT-ITMS experiments. For example, a plot of the experimental frequencies for the characteristic ions m/z 120, 105, 77, 65, and 43 of acetophenone and the theoretical values for an ideal quadrupole field calculated using the Mathieu equations, is shown in Fig. 7. Note that the frequencies were calculated from q_z using a computer program [18] which calculates β_z from q_z using the continuing fraction relationship between these terms [16]. The experiment employed dc excitation and FT detection, with acetophenone as sample. The observed frequencies for the sample ions m/z 120, 105, 77, 51, 43 are plotted against their theoretical values as calculated using the Mathieu equation for a pure quadrupole field. This shows the typical nature of the shifts observed in these experi-

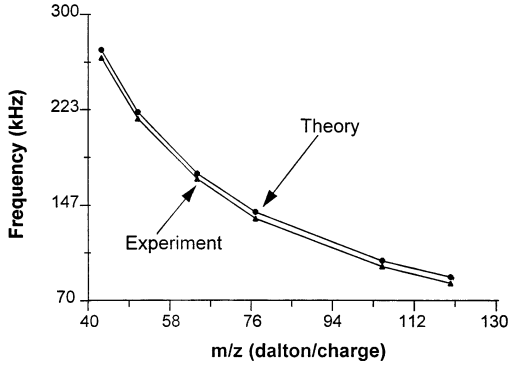

Fig. 7. Correlation between experimental (observed) and theoretical frequencies for acetophenone m/z 120, 105, 77, 65, 51, and 43 ions. Low mass/charge cutoff, m/z 30; ionization time, 1 ms; broadband excitation by dc pulse, 23 V, 2 μs; nominal sample pressure, 9×10^{-7} Torr.

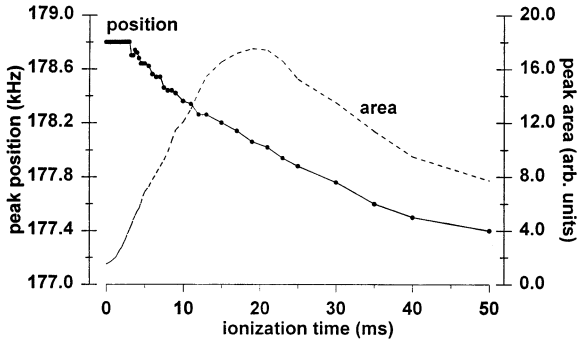

Fig. 9. The influence of space charging on peak position and peak area is shown for m/z 40 ions of argon. Low mass cutoff, m/z 20; ionization time, variable; nominal sample pressure, 2×10^{-6} Torr; excitation by dc pulse, 8 V, 2 μs. The peak position and areas were measured using the digital scope.

ments. Experiments were also performed as a function of rf voltage (low mass cutoff) to see the effect on peak position. A constant shift was observed between the experimental and theoretical frequency values under fixed operating conditions, as shown in data for argon (m/z 40) (Fig. 8). In this experiment, the Ar^+ ion (m/z 40) frequency was measured at different rf trapping voltages expressed as the low mass-to-charge ratio cutoff values. The observed frequency values are plotted against the theoretical values.

Optimization and control of experimental parameters, especially pressure and ionization time, is required to achieve such correlations. The frequency

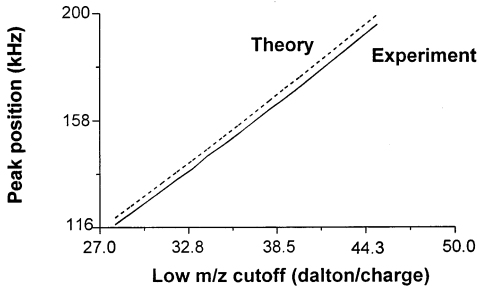

Fig. 8. Plot showing the systematic shift between the observed versus theoretical frequencies for argon (m/z 40) ions as a function of the low m/z cutoff (rf voltage). Ionization time, 10 ms; broad-band excitation by dc pulse, 35 V, 2 μs; nominal sample pressure, 2×10^{-6} Torr.

shifts increased when larger ion populations were studied, presumably due to space charging as discussed below.

Shifts due to space charging

The performance of the ion trap is dependent upon the number of trapped ions [16]. As this number increases, the total ion cloud charge produces a defocusing field that is superimposed on the trapping quadrupolar field [19–21]. There are also important effects that have been described as local space charge effects, which depend on the number of ions with mass similar to that of the ion(s) of interest [22]. Several authors [22–24] have shown that space charging induces coupling of motion between populations of ions of different masses. Because FT-ITMS involves direct measurement of ion frequencies, space-charge-induced shifts can be directly observed. Fig. 9 shows the influence of increasing the ion number on the peak position (frequency) and peak area for argon, Ar^+ ions (m/z 40). The plot indicates that the ion secular frequency decreases as the space-charge increases, as is well known from theory [19, 20, 25]. The peak area increases with ionization time, as expected, except at long ionization times when space charge effects are large enough to degrade the signal. The loss of resolution that accompanies coupling of ion motion from space charging can be seen in the data shown in Fig. 10. The spectra, which show the

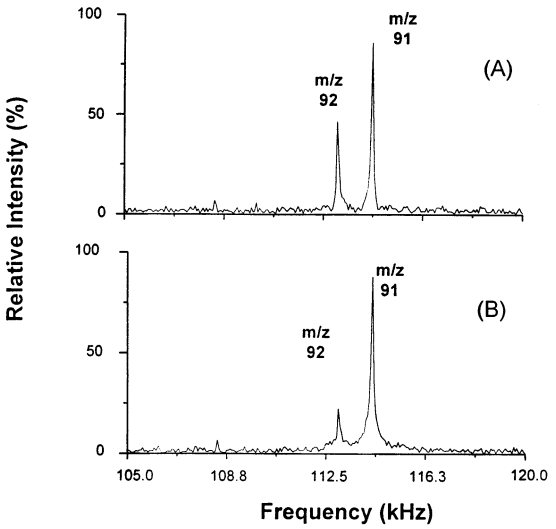

Fig. 10. Influence of space-charging on resolution of adjacent masses (m/z 91 and 92) of *n*-butylbenzene. Low mass cutoff, m/z 25; ionization time, 10 ms (A), 30 ms (B); nominal sample pressure, 9×10^{-7} Torr; narrow-band ac excitation 113.8 kHz, 0.25 V, 100 μs.

ions m/z 91 and 92 of *n*-butylbenzene, were recorded using narrow-band ac excitation at a sample pressure of 9×10^{-7} Torr and ionization times of 10 ms (Fig. 10A) and 30 ms (Fig. 10B). At the higher ionization time, the less abundant m/z 92 peak shifts towards the more abundant m/z 91 peak by about 200 Hz, a result similar to that observed in a conventional destructive-detection experiment [22]. There is also a widening of the peak base, hence a loss of resolution, because the loss of coherence as a result of ion–ion interactions.

The frequency shift is related quantitatively to the number of trapped ions as this affects the iso-β values on which secular frequencies depend. According to Schwebel and co-workers [26], ion concentrations (N_i) can be calculated based on the difference between the theoretical $\omega_{0(\text{theo})}$ and the experimental $\omega_{0(\text{expt})}$ values of the secular frequencies as follows:

$$N_i = (3\epsilon_0 m/2e)|(\omega_{0(\text{theo})})^2 - (\omega_{0(\text{expt})})^2| \qquad (10)$$

Eq. (10) yields an approximate ion density of 5×10^4 cm^{-3}, which applies to an experiment in which S/N = 50 and this result is consistent with the estimate made above, that a few thousand ions give S/N of unity. Note, however, that this estimate is only approximate as field imperfections also cause frequency shifts (see below).

Shifts due to nonlinear resonances

The presence of higher-order fields in ion traps and their influence on ion trap performance has been well documented [16,27]. In a hypothetical "ideal" ion trap, a pure (100%) quadrupolar field exists and its strength varies linearly along the spatial coordinates x, y, and z. Ideally, the ion axial and radial frequency components are independent of each other and of the ion position. However, due to misalignments, deviations from ideal hyperbolic shape, truncation, and imperfections in the spacing of electrodes in real ion traps, there is a superimposition of weak higher-order multipoles (mainly octopoles and hexapoles) on the quadrupole field. This effect is empirically corrected for in the extended geometry ($r_0 = 1.000$ cm, $z_0 = 0.783$ cm) Finnigan trap used here. However, higher-order field components remain and this makes the ion frequency dependent upon the axial and radial position of the ion cloud. Nonlinear (higher-order field) resonances which occur at particular values of β_z and $\beta_{r,}$ and hence at particular working points on the stability diagram, have also been reported [24,28,29]. Nonlinear fields cause a coupling between the ion axial and radial motions and this also distorts the shape of the ion resonance absorption peak [30, 31]. In addition to causing frequency shifts, higher-order field resonances may cause ions to be accelerated towards the electrodes, resulting in ion loss. The use of a single-detector electrode in the FT ion trap introduces an asymmetric distortion in the field that is expected to result in a significant percentage of hexapole field. This, together with the position dependence of the ion secular frequency, further complicates the frequency shift problem in FT-ITMS. In practice, the hyperbolic shape of the endcap electrodes, as compared to ideal flat, parallel plates, further alters the shape, magnitude, and frequency of the excitation field (as contrasted with the trapping field) and can also contribute to frequency shifts.

The contributions from various nonlinear contributions are difficult to study and quantify. However,

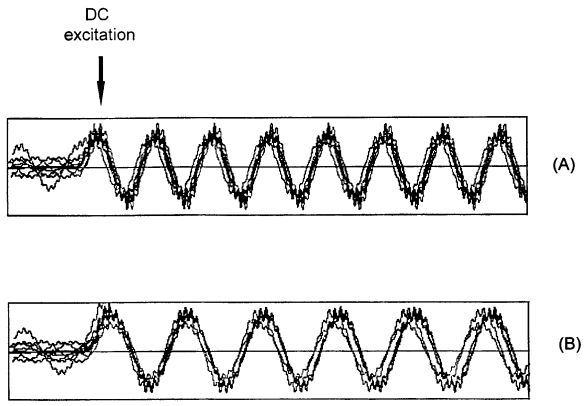

Fig. 11. Simulations of ion axial trajectory under (A) ideal and (B) nonlinear conditions is shown. The phase coherence caused by dc excitation is lost under nonlinear conditions in B.

computer simulations of ion motion can be used to study the influence of higher-order fields on the peak position and resolution. We have used ITSIM, an ion trap simulations program developed in our laboratory, for such studies [32]. The inhomogeneity of the quadrupole field is considered to be the only nonlinear factor in the results described below, i.e. no space charge effects are considered. Figs. 11A and 11B show simulated ion trajectories in the axial dimension for a collection of 10 ions of m/z 40 (argon) at q_z = 0.227, for an ideal trap (pure quadrupole field, z_0 = 0.707 cm) and a nonlinear trap, respectively. The nonlinear trap has r_0 = 1.00 cm, z_0 = 0.783 (stretched trap geometry), and this is assumed to contribute 1.4% octopole and 3% hexapole fields, as calculated using the program POISSON [33]. In both cases, the ions are excited by a 4 V, 3 μs wide dc pulse to cause coherent oscillations with large amplitudes. The coherence achieved is maintained under ideal conditions (Fig. 11A) but progressively deteriorates in the nonlinear device (Fig. 11B). This dephasing is due to the position-dependent shift in the secular frequency caused by the higher multipoles. Note that these effects occur when ions of a single mass-to-charge ratio value are trapped and are independent of ion/ion repulsions that have not been considered.

In cases where ions of different masses are simulated, the frequency shift and frequency coupling induced by the higher-order fields become even more evident. Fig. 12 shows the simulated frequency spectra of m/z 84 and 86 ions (krypton) at a q_z value of 0.27. Two ion trajectory simulations, one for an ideal trap and the other for a nonlinear trap, were performed using parameters identical to those used for Fig. 11. The frequency spectra were obtained by Fourier transforming the ion trajectory data. Simulations for the ideal trap (Fig. 12A) yield the expected peak positions (106.5 and 104.0 kHz) and separation (2.5 kHz) for the two masses at given q_z values. However, introduction of nonlinear conditions causes the peaks to shift differentially to lower frequencies, resulting in loss of resolution (Fig. 12B). The magnitudes of the

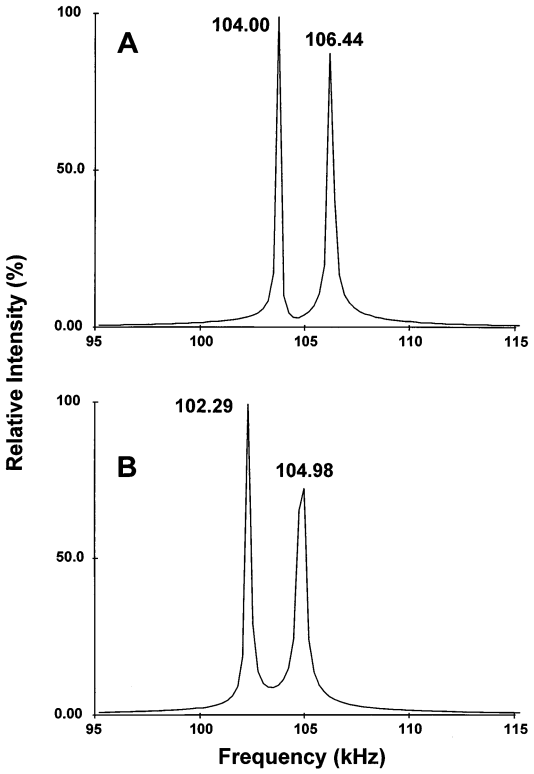

Fig. 12. The effect of higher-order fields on peak position and spacing is shown in the form of simulated mass spectra of m/z 84 and m/z 86 ions of krypton under ideal (A) and nonlinear (B) conditions. One ion each of m/z 84 and 86, initial position randomly chosen from a gaussian distribution (σ = 5 mm) is trapped at q_z = 0.27 and q_z = 0.264, respectively. The higher order fields are 1.4% octapole and 3% hexapole.

higher-order fields used in Fig. 12 are exaggerated for clarity. The quadrupolar component reflects the stretching of the trap and the hexapolar component, the asymmetry associated with the pin electrode.

Mass calibration

Characterizing the nature of the frequency shifts is difficult due to the interdependent space charge and nonlinear resonance effects just discussed and the strong dependence of the data on experimental conditions. An empirical approach based on experimental data (e.g. Fig. 7) is therefore used for mass calibration. From the solution to the Mathieu equations it is known [16] that the mass-to-charge ratio value of an ion is inversely related to its secular frequency ω_z:

$$\frac{m}{z} = \frac{8V}{q_z(r_0^2 + 2z_0^2)\Omega^2} \tag{11}$$

for $a_z = 0$ and $q_z < 0.4$

$$\omega_z = \frac{\beta_z \Omega}{2}, \text{ where } \beta_z = \frac{q_z}{\sqrt{2}} \tag{12}$$

Thus,

$$\frac{m}{z} = \left(\frac{4V}{(r_0^2 + 2z_0^2)\sqrt{2}\Omega}\right)\frac{1}{\omega_z} \tag{13}$$

or

$$\frac{m}{z} = A\frac{1}{\omega_z}, \tag{14}$$

where r_0 and z_0 are the radial and axial dimensions, a_z, q_z and β_z are the Mathieu parameters, V is the zero-to-peak magnitude of the rf voltage, and Ω is its frequency. The value of the correlation coefficient, A, is determined experimentally and fitted using a quasilinear regression algorithm.

Mass resolution

The peak width is inversely proportional to the length of the acquired transient (assuming no peak broadening by collisions or nonlinear resonances). For a 20 ms transient, this precision of frequency measurement is limited to 50 Hz. However, space charge and nonlinear resonances occur in these experiments and cause additional peak broadening. Experiments under different operating conditions produced peak widths [full width at half maximum (FWHM)] ranging from 150 to 250 Hz. However, under given experimental conditions, the widths of the peaks were approximately constant. Because frequency increases with decreasing mass-to-charge ratio, the resolution ($f_z/\Delta f_z$) is expected to be highest at low mass-to-charge ratio. The frequency separation between ions of consecutive masses is not constant across the mass range for a fixed set of conditions. Ions with lower frequencies (higher mass-to-charge ratios) are more closely spaced than ions at higher frequencies. Hence, resolving ions of low mass-to-charge ratios is easier than resolving high mass-to-charge ratio ions. Similar considerations apply in FT-ICR [34].

The use of higher pressures leads to more collisions between the ions and neutral molecules and this causes a decrease in the time taken for exponential decay of the coherence in the time-domain waveform. This shortens the length of the transient and broadens the peaks in the frequency domain. Thus, it is desirable to detect the ions at low pressures. However, internal ionization methods as used here require higher pressures. The requirement for adequate sample and low operating pressure are mutually incompatible although pulsed gas introduction previously implemented with ion traps [35] should be valuable in optimizing the conditions. The effect of pressure on transient lifetimes was studied using krypton ions (m/z 84) (Fig. 13). Transient lifetimes were determined at nominal sample pressures of 2, 3 and 5×10^{-6} Torr. The transient length was measured by acquiring the signal at various times after dc excitation. The plot shows that the longest transients, 23 ms, were obtained at the lowest pressure, as expected.

Higher resolution can be obtained using the narrow-band detection mode. This method is analogous to the use of slow scan rates to achieve high resolution in mass-selective instability experiments: high resolution is only obtained by slowing the scan rate to the point where only a narrow mass range can

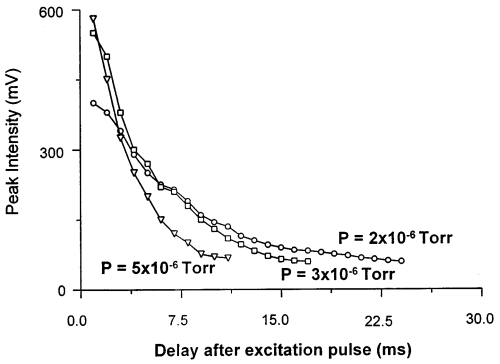

Fig. 13. The effect of pressure on the length of the transient (transient lifetime) is shown by a plot of signal intensity versus time. The longest transient (23 ms) is obtained at lowest pressures (2×10^{-6} Torr). Low mass/charge cutoff, m/z 40; ionization time, 10 ms; excitation by dc pulse, 65 V, 2 μs.

be scanned [36]. The scan rate and resolution are inversely related; hence, the slower the scan the higher the resolution. FT-ITMS, on the other hand, has the potential to provide high resolution spectra in a relatively shorter amount of time and over a much wider mass range. An $f_z/\Delta f_z$ resolution of about 1000 (unit mass) was found to be routine in the broadband mode whereas narrow-band detection experiments [7] provided a higher resolution, in excess of 3000.

dc biasing during nondestructive detection

The S/N ratio can be increased by manipulating the center of the ion oscillating orbit using small dc offset voltages applied to the endcap electrode bearing the detector, as shown in Fig. 14. When the dc offset potential on the endcap is varied, the signal intensity and peak position change as shown for Kr^+ (m/z 84) ions in Fig. 15. The observed gain in intensity is due to the use of the single-detector electrode configuration (single-ended detection) and is expected to cancel out in the dual-detector electrode (differential detection) configuration discussed below. It is known from studies on nonlinear fields [27] that hexapolar fields are associated with asymmetry of the ion trap geometry (like the present modification) and thus cause a shift in the ion cloud center. It may thus be possible to apply an appropriate dc offset voltage and correct for

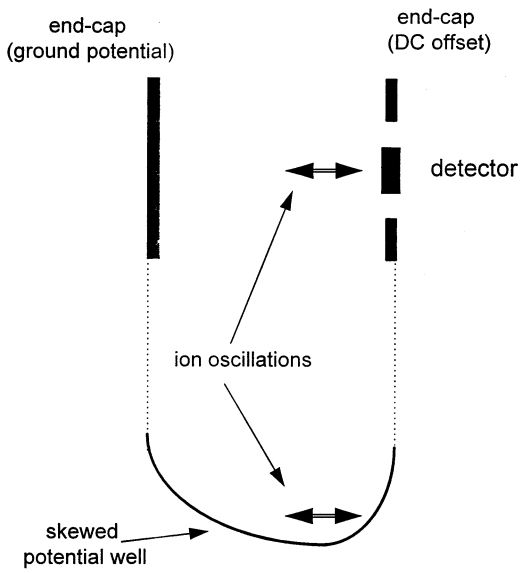

Fig. 14. The shifting of ion cloud oscillation center due to dc biasing of the endcap electrode is depicted in this schematic.

such shifts. It may also be possible to use dc biasing for mass calibration purposes. More detailed studies need to be performed before any practical applications of dc biasing in nondestructive detection are possible.

Dual-detector electrode configuration

An alternative electrode configuration should improve the performance of FT-ITMS. This dual-detector electrode configuration, shown in Fig. 16, should allow true differential detection of the image current. This should minimize the systematic noise in the system, including the rf pickup. The rf signal pickup at the two detector electrodes can be nulled at the preamp input using differential detection. This would be especially useful in ion remeasurement experiments [13] where the high systematic background currently prevents us from obtaining the expected gain in the S/N ratio. Dual-ended detection should also minimize the even-order harmonics observed in the current experiments and provide the expected 2× gain in sensitivity. Another advantage of this design is the re-establishment of the ion trap symmetry. As mentioned above, the asymmetric (single detector

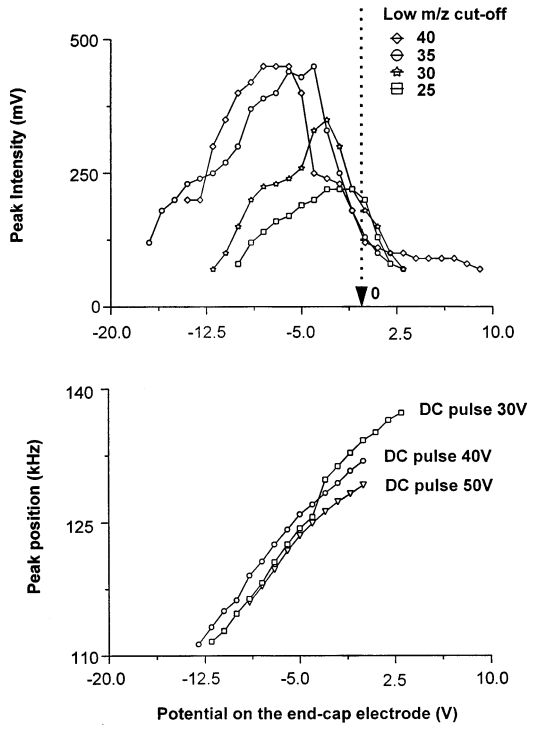

Fig. 15. Results from the dc biasing experiment showing the variation in peak position and intensity as a function of dc bias voltage. The upper plot is taken at the low mass/charge cutoff values shown, the lower at a value of 30 Da/charge. The upper plot is taken using excitation with a 30 V, 2 μs dc pulse, the lower with the amplitudes shown; nominal sample pressure, 2×10^{-6} Torr.

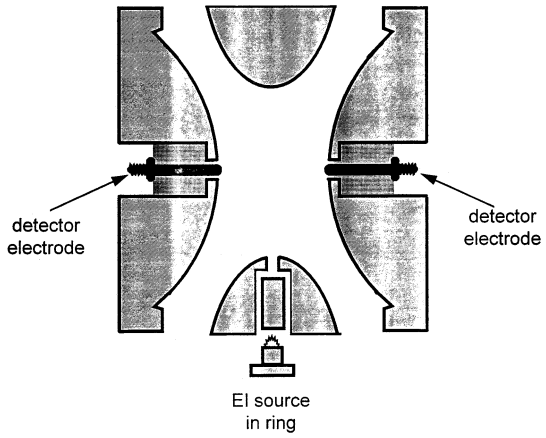

Fig. 16. An ion trap design showing dual detector electrodes for improving the performance of FT-ITMS. Ionization can be carried out for example, using an EI source mounted on the ring electrode.

electrode) design introduces strong (nonlinear) hexapolar fields. The dual-detector configuration would eliminate this asymmetry and minimize the deleterious effects of hexapolar resonances.

Conclusions

In this article we have addressed important issues like frequency shifts, mass calibration, sensitivity, and mass resolution in broadband FT-ITMS. Details of the experimental arrangement and detection circuitry are provided. Space charge induced effects on peak position and resolution are discussed with the help of experimental data on argon and *n*-butylbenzene recorded as a function of ionization time. Ion frequencies are found to shift to lower values whereas adjacent peaks merged as the ionization time was increased. Nonlinear fields also play a role in causing frequency shifts and in resolution and sensitivity loss. Some of these effects were investigated by using computer simulations of ion motion with and without higher order fields. Loss of phase coherence, due to shifting secular frequencies, was observed in ion axial trajectory simulations under nonlinear conditions. Frequency shifts are accompanied by coupling of motion between adjacent ions due in part to nonlinear field contributions. The cumulative influence of space charging and nonlinear fields make mass calibration difficult. Therefore, correlations between experimentally observed and theoretical calculated frequencies were used to obtain an approximate mass calibration law. Experimentally, resolutions of 1000 and 3000 are routinely obtained in the broadband and narrow-band modes of nondestructive detection, respectively. A means of altering the position of the ion orbit during ion detection was investigated using dc bias voltages. Significant changes in peak positions (frequencies) and intensities were observed in this experiment.

Further experiments are underway to better understand and improve the performance of the FT-ion trap. Differential detection of the image currents using dual detector trap should improve S/N ratios by eliminating systematic noise and minimizing second-order

harmonics and the effects of the asymmetric field distortions caused by the unsymmetrical single-detector electrode geometry. Pulsed introduction of the sample [35] should improve performance by lengthening the transient signal. Electronic rf nulling at the preamp input and better shielding from environmental noise and noise from the EI source are also being considered to improve performance at high rf voltages. Phase locking of the excitation signals (ac and dc) with the rf is another option that will allow better control over ion excitation, especially in remeasurement experiments. A data acquisition system that incorporates digital signal-processing methods commonly used in FT-ICR, including zero-filling, apodization, and summing, is being developed for better data handling and processing.

Acknowledgements

This work was supported by the US Department of Energy, Office of Basic Energy Sciences, and by Finnigan Corporation. We thank Jonathon W. Amy, Huy Bui, Robert A. Santini, and Weldon Vaughn for technical assistance and valuable discussions.

References

[1] W. Paul, H.P. Reinhard, U. Von Zahn, Z. Phys. 152 (1958) 143.
[2] E. Fischer, Z. Physik 156 (1959) 1.
[3] G. von V. Rettinghaus, Z. Angew. Physik 22 (1967) 321.
[4] J.H. Parks, S. Pollack, W. Hill, J. Chem. Phys. 101 (1994) 6666.
[5] D.E. Goeringer, R.I. Crutcher, S.A. McLuckey, Anal. Chem. 67 (1995) 4164.
[6] G.C. Stafford Jr., P.E. Kelley, J.E.P. Syka, W.E. Reynolds, J.F. Todd, Int. J. Mass Spectrom. Ion Processes 60 (1984) 85.
[7] M.H. Soni, V. Frankevich, M. Nappi, R.E. Santini, J. Amy, R.G. Cooks, Anal. Chem. 68 (1996) 3314.
[8] A.G. Marshall, T.C. Wang, T.L. Ricca, Am. Chem. Soc. 107 (1985) 7893.
[9] R.K. Julian Jr., R.G. Cooks, Anal. Chem. 65 (1993) 1827.
[10] J.E.P. Syka, W.J. Fies, Jr., Proceedings of the 35th ASMS Conf. Mass Spectrom. Allied Topics, Denver, CO, May 1987, p. 767.
[11] M.B. Comisarow, A.G. Marshall, Chem. Phys. Lett. 25 (1974) 282.
[12] E. Williams, K. Henry, F.W. McLafferty, J. Am. Chem. Soc. 112 (1990) 6157.
[13] M.B. Comisarow, J. Chem. Phys. 69 (1978) 4097.
[14] J.N. Louris, R.G. Cooks, J.E.P. Syka, P.E. Kelley, G.C. Stafford, J.F.J. Todd, Anal. Chem. 59 (1987) 1677.
[15] M.H. Soni, R.G. Cooks, Anal. Chem. 66 (1994) 2488.
[16] R.E. March, J.F.J. Todd, Practical Aspects of Ion Trap Mass Spectrometry: Vol. 1–3, CRC, New York, 1995.
[17] J.E.P. Syka, W.J. Fies Jr., U.S. Patent 4755670 (1988).
[18] J.N. Louris, Ph.D. thesis, Purdue University, 1993.
[19] C. Schwebel, P.A. Moller, P.T. Manh, Rev. Phys. Appl. 10 (1975) 227.
[20] J.F.J. Todd, R.M. Waldren, D.A. Freer, R.B. Turner, Int. J. Mass Spectrom. Ion Processes 35 (1980) 107.
[21] J.V. Johnson, R.A. Yost, P.E. Kelley, D.C. Bradford, Anal. Chem. 62 (1990) 2162.
[22] K.A. Cox, C.D. Cleven, R.G. Cooks, Int. J. Mass Spectrom. Ion Processes 144 (1995) 47.
[23] W. Mo, J.F.J. Todd, Rapid Commun. Mass Spectrom. 10 (1996) 424.
[24] D.M. Eades, R.A. Yost, Rapid Commun. Mass Spectrom. 6 (1992) 573.
[25] F. Vedel, J. Andre, Phys. Rev. 29 (1984) 2098.
[26] P.A. Moller Manh, P.-T. Schwebel, C. Schwebel, Rev. Phys. Appl. 10 (1975) 227.
[27] J. Franzen, R. Gabling, M. Shubert, Y. Wang, Non-linear Ion Traps, Chap. 3 in [16], Vol. 1.
[28] K.L. Morand, S.A. Lammert, R.G. Cooks, Rapid Commun. Mass Spectrom. 5 (1991) 491.
[29] R. Alheit, S. Kleineidam, F. Vedel, M. Vedel, G. Werth, Int. J. Mass Spectrom Ion Processes 154 (1996) 155.
[30] Y. Wang, Rapid Commun. Mass Spectrom. 7 (1993) 920.
[31] J.F.J. Todd, A.D. Penman, D.A. Thorner, R.D. Smith, Rapid Commun. Mass Spectrom. 5 (1991) 491.
[32] H.P. Reiser, R.K. Julian, R.G. Cooks, Int. J. Mass Spectrom. Ion Processes 121 (1992) 49.
[33] J.H. Billen, L.M. Young, Proceedings of the 1993 Particle Accelerator Conference, 1993, Vol. 2, pp. 790–792.
[34] I.J. Amster, J. Mass Spectrom. 31 (1996) 1325.
[35] W.B. Emary, R.E. Kaiser, H.I. Kenttamaa, R.G. Cooks, J. Am. Soc. Mass Spectrom. 1 (1990) 308.
[36] J.C. Schwartz, J.E.P. Syka, I. Jardine, J. Am. Soc. Mass Spectrom. 2 (1991) 198.